Chemical Science

ROYAL SOCIETY OF CHEMISTRY

EDGE ARTICLE

View Article Online
View Journal | View Issue

Check for updates

Cite this: *Chem. Sci.*, 2025, **16**, 13267

All publication charges for this article have been paid for by the Royal Society of Chemistry

Received 16th January 2025
Accepted 11th June 2025

DOI: 10.1039/d5sc00394f

rsc.li/chemical-science

Optimal photosynthesis of 2-benzothiazoles over hexaazatrinaphthylene-based porous aromatic frameworks†

Jingjing Shao, He Wang, Xin Tao * and Guangshan Zhu

Porous aromatic frameworks (PAFs) are considered as promising photocatalysts for efficient organic transformations. In this study, the synthesis of donor–acceptor (D–A)-type hexaazatrinaphthylene-based porous aromatic frameworks (HATN-PAFs) is presented. By linking HATN units with other different fragments, the surface areas, bandgaps, energy levels and photoelectric properties of HATN-PAFs could be easily tuned. Notably, the combination of HATN with triphenylamine (TPA) fragments facilitates photoinduced charge separation and migration, and reactant transport and activation during photocatalysis, which achieves high yields (up to 99%), an expandable substrate scope (20 examples), and good recyclability (up to 10 cycles) for the photosynthesis of 2-benzothiazoles under an air atmosphere upon excitation by a blue LED light (460 nm, 24 W). This photocatalytic system does not require additional oxidants or metals, making it environmentally friendly. A mechanistic study reveals that the simultaneous generation of the reactive oxygen species $O_2^{\bullet-}$ and $^1O_2$ over this catalytic system may jointly accelerate the oxidative formation of 2-benzothiazoles.

Introduction

Benzothiazole derivatives are valuable organic building blocks in pharmaceutical chemistry, materials science and other fields. Specifically, 2-arylbenzothiazole and its derivatives are essential structural and functional units of various pharmaceutical intermediates with excellent physiological and pharmacological properties,[1–4] which are widely used in antibacterial drugs,[5,6] anti-inflammatory agents,[7,8] antitumor agents[9] and so on. Therefore, developing efficient synthesis methods for 2-arylbenzothiazole derivatives is particularly attractive.

Until now, various catalytic technologies such as thermal catalysis, electrocatalysis and photocatalysis have been employed for the synthesis of benzothiazole derivatives (Scheme 1). The traditional thermally induced synthesis of 2-arylbenzothiazole derivatives is usually achieved under harsh reaction conditions, such as those involving high temperatures and toxic metal catalysts, leading to high energy consumption, low selectivity and serious environmental concerns.[10–14] Emerging electrocatalysis techniques could overcome these problems, but they usually require the use of expensive electrodes.[15] In contrast, visible-light-driven photocatalytic transformations provide a greener and more sustainable approach for 2-arylbenzothiazole synthesis.[16–18] Thus, various organic dye molecules (fluorescein,[19] enzymes,[20] and vitamins[21]) have been widely applied for the photocatalytic synthesis of 2-arylbenzothiazole derivatives. However, separating and reusing these

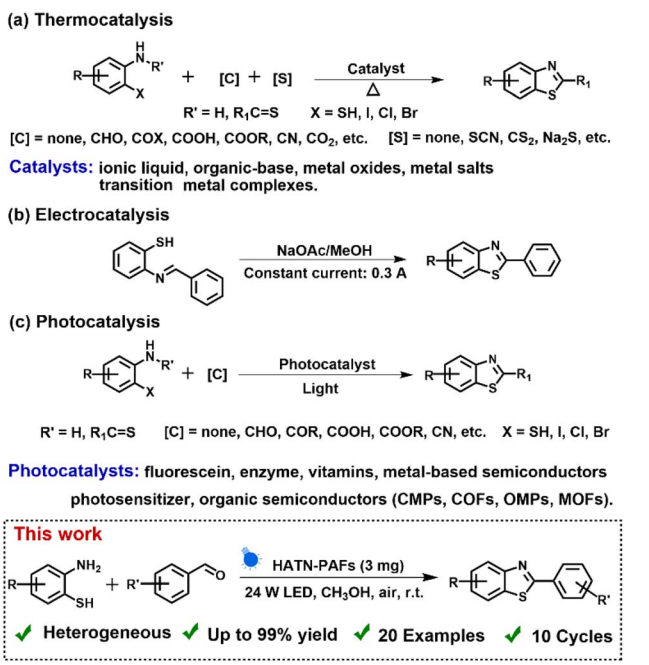

Scheme 1 The synthetic routes to benzothiazole derivatives.

Key Laboratory of Polyoxometalate and Reticular Material Chemistry of Ministry of Education, Faculty of Chemistry, Northeast Normal University, Changchun 130024, China. E-mail: taox091@nenu.edu.cn

† Electronic supplementary information (ESI) available. See DOI: https://doi.org/10.1039/d5sc00394f

homogeneous photocatalysts have been highly challenging. On the other hand, metal-based heterogeneous photocatalysts such as nonprecious metal-based semiconductors (CdS,[22] CdSe-MMT[23] and TiO_2 [24]) and metal–organic frameworks (MOFs)[25] usually exhibit insufficient stability in the process of 2-arylbenzothiazoles photosynthesis. Recently, organic semiconducting materials such as conjugated microporous polymers (CMPs),[26] ordered mesoporous polymers (OMPs)[27] and covalent organic frameworks (COFs)[28,29] have been investigated as heterogeneous photocatalysts for 2-arylbenzothiazole synthesis, due to their tuneable local structures and photoelectric properties. However, these photocatalytic processes require a pure oxygen atmosphere and/or long reaction times, which greatly limits their practical applications. Therefore, it is of great significance to develop porous organic photocatalytic materials with high catalytic efficiency and good recyclability for the photosynthesis of 2-arylbenzothiazole derivatives.

Recently emerging porous aromatic frameworks (PAFs) have been proved to be promising candidates to serve as efficient and stable photocatalysts, due to their tunable local structures, robust chemical bonding, and high specific surface areas.[30–32] Constructing PAF materials with regulated optical bandgaps, suitable energy levels, abundant active sites and appropriate durability is of great interest. To achieve this goal, an effective method is the combination of suitable molecular fragments with unique electronic and geometric structures by efficient carbon–carbon bond formation reactions to construct PAFs those are satisfactory for specific photo-reactions.[33] Specifically, π-conjugated PAFs with alternating electron donors (D) and acceptors (A) could be formed by this method, which usually facilitate the efficient separation and transfer of photogenerated charge carriers.[34] Therefore, PAFs have served as efficient photocatalysts for organic transformations such as benzimidazole synthesis,[35,36] H_2O_2 production,[37,38] the decontamination of mustard gas simulant,[39] CO_2 conversion[40] and energy storage.[41] In addition, hexaazatrinaphthylene (HATN) is a well-known dinaphthalene-type pyrazine-based compound, which is recognized for its photochemical stability, high electron affinity, ease of functionalization and high electrical conductivity.[41–43] Previously, a HATN-based porous aromatic framework (HATN-PAF) has been reported to serve as the cathode material for self-recharging aqueous Zn–K hybrid ion batteries.[41] The unique features of HATN-PAF materials encourage us to further optimize their structures to serve as efficient photocatalysts for specific reactions. The rigid planar heterocyclic redox active centre with π-conjugation from the HATN fragment may favour photoinduced electron–transfer reactions. Moreover, HATN derivatives have remarkable electron-deficient properties, which makes them suitable to serve as electron-acceptor components in D–A type semiconducting porous materials.[44] In this study, three nitrogen-rich molecular fragments with different electron donating abilities, triphenylamine (TPA), 2,4,6-triphenyltriazine (TPTA) and 1,3,5-triphenylbenzene (TPB), were coupled with HATN to construct three C–C-bond-linked D–A-type HATN-PAFs, named PAF-406, PAF-407 and PAF-408 (Scheme 2). By changing

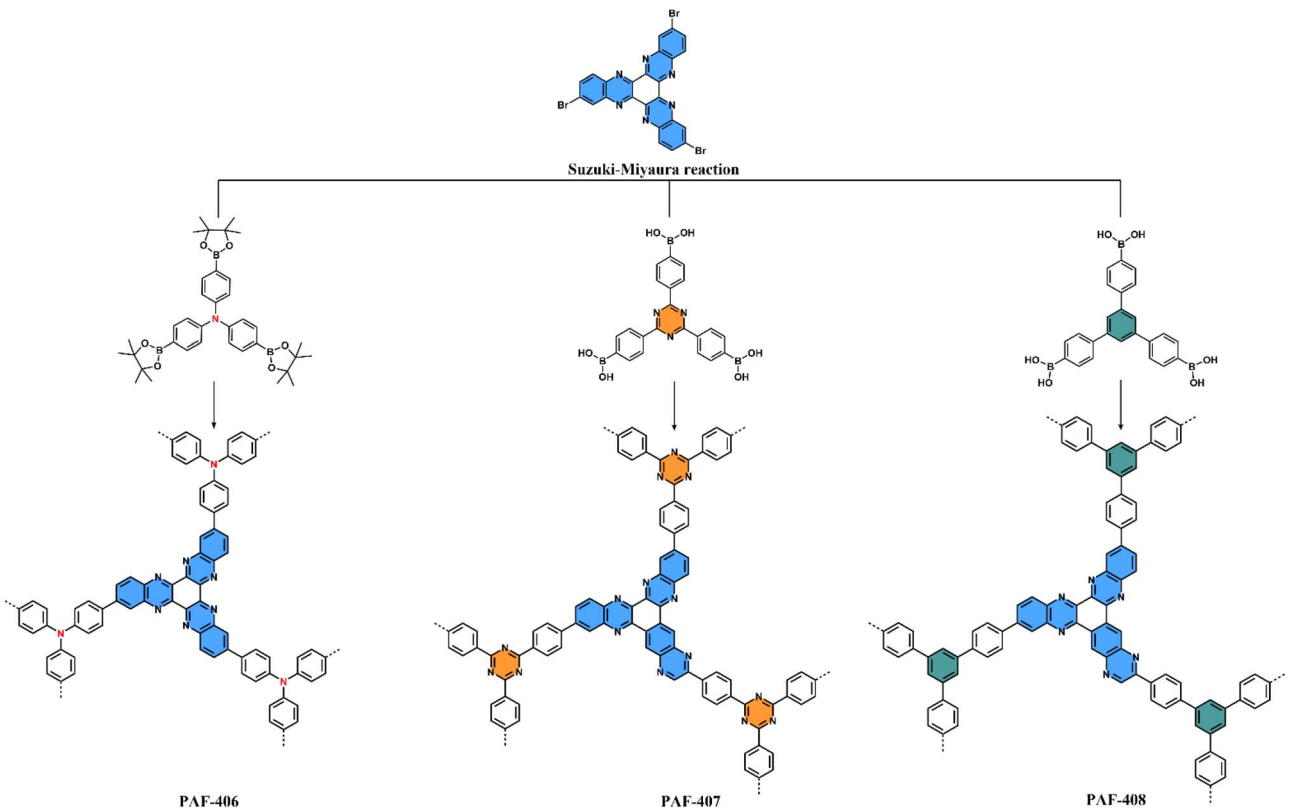

Scheme 2 The synthesis of HATN-PAFs.

different types of D fragments, the band gaps, energy levels, and photoelectric properties of these HATN-PAFs can be tuned to activate oxygen to generate the reactive oxygen species $O_2^{\bullet-}$ and $^1O_2$. This promotes the photosynthesis of benzothiazoles in excellent yields with broad substrate applicability and good recyclability under ambient conditions, which is superior to previously reported organic semiconductors.

Results and discussion

Synthesis and characterization of HATN-PAFs

HATN-PAFs were synthesized *via* efficient cross-coupling reactions of tribromo-substituted hexaazatrinaphthylene (HATN-Br) with boron-derived TPA, TPTA and TPB fragments in the presence of $Pd(PPh_3)_4$ under solvothermal conditions, with the resulting materials named PAF-406, PAF-407 and PAF-408, respectively (Scheme 2).[45,46] The chemical compositions of the obtained HATN-PAFs are further characterized by various techniques. It is found that the characteristic vibrational signals of the HATN fragments are maintained in the Fourier transform infrared (FT-IR) spectra of HATN-PAFs (Fig. 1a). The strong signals from the C–N bonds in PAF-406 appear at around 1321 cm^{-1}.[47] The strong bands from the C=N bonds of the triazine ring in PAF-407 are located at around 1511 and 1356 cm^{-1}.[48] The C–Br bond signals (around 579 cm^{-1}) observed for the edge of the networks in HATN-PAFs are weakened compared to monomeric HATN-Br.[49] X-ray photoelectron spectroscopy (XPS) analysis of the HATN-PAFs, in comparison with their synthetic monomers, shows that the C 1s peaks of the HATN-PAFs can be deconvolved into four major characteristic peaks. The peaks at 284.8 and 285.8 eV could be assigned to the C=C/C–C and C–N=C bonds, respectively.[50,51] Additionally the peaks at 285.1 and 287.1 eV in the C 1s spectra could be attributed to C–N and C=N bonds, respectively (Fig. S1 and S2†).[49,52] In the N 1s XPS spectra, the peaks at 398.7, 399.9 and 399.3 eV can be attributed to N=C, N–C and C–N=C, respectively (Fig. S3 and S4†).[49,53] In the O 1s and B 1s XPS spectra, HATN-PAFs do not display characteristic signals at 531.0 or 190.9 eV, indicating the absence of boronic acid groups in HATN-PAFs (Fig. S5–S8†).[54,55] The chemical structures of HATN-PAFs are further investigated in comparison with their constituent molecules (*i.e.* HATN, TPA, TPTA and TPB) by ^{13}C cross polarization magic angle spinning (CP-MAS) solid-state NMR spectroscopy (Fig. 1b and S9†). The ^{13}C signals observed at around 142 ppm in these three HATN-PAFs belong to the carbon atoms of the central hexa-substituted benzene rings in the HATN fragments,[56,57] which is comparable to what is observed for HATN molecules. The ^{13}C signals in the range of 120–140 ppm could be tentatively assigned to the carbon atoms of di- and tri-substituted or fused benzene rings, similar to those observed for HATN, TPA, TPTA and TPB.[56,58] Specifically, in the solid-state ^{13}C NMR spectrum of PAF-406, the phenylene carbons neighboring nitrogen atoms in TPA fragments appear at 148 ppm, which is consistent with what is observed for TPA molecules.[56,59] The carbon signal from the triazine core is observed at about 171 ppm in the solid-state ^{13}C NMR spectrum of PAF-407, which is confirmed by comparison with that of TPTA molecules.[56,60] All this evidence demonstrates the inclusion of the key molecular fragments in HATN-PAFs. The permanent porosity properties of PAF-406, PAF-407 and PAF-408 are assessed by N_2 sorption measurements at 77 K (Fig. 1c). PAF-406 has a higher Brunauer–Emmett–Teller (BET) specific

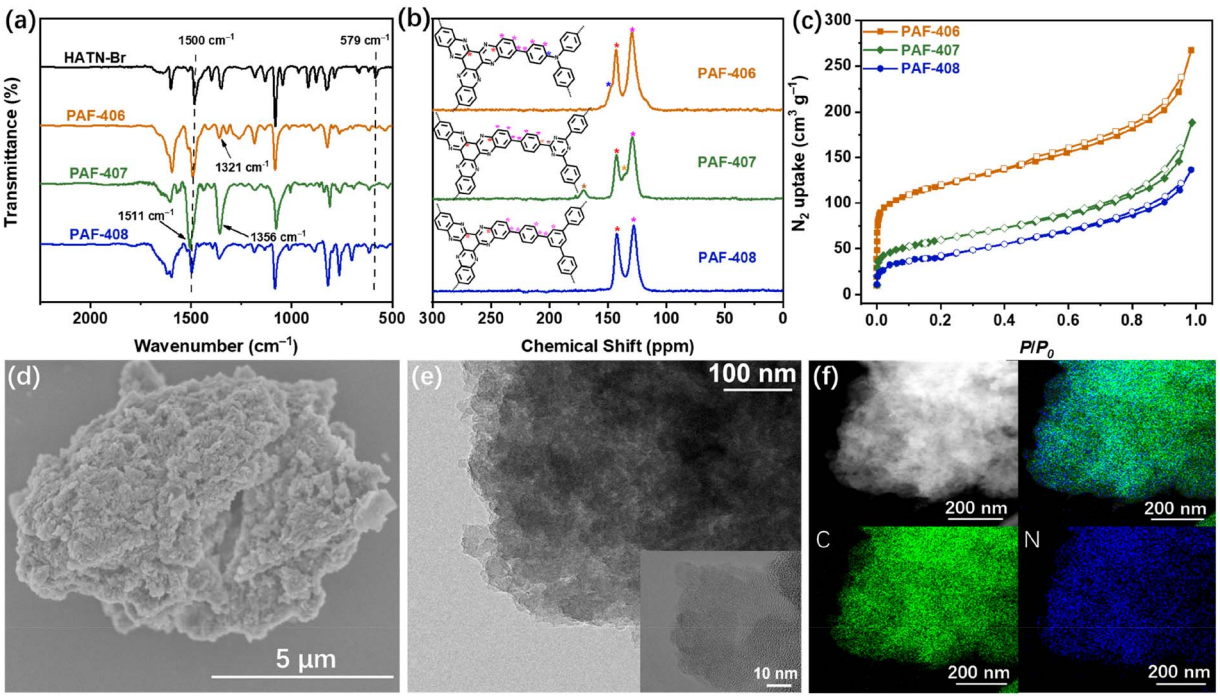

Fig. 1 (a) FT-IR spectra. (b) Solid-state ^{13}C CP-MAS NMR spectra. (c) N_2 adsorption/desorption isotherms at 77 K. (d) An SEM image of PAF-406, (e) TEM images of PAF-406, and (f) TEM elemental mapping of PAF-406 showing carbon (green) and nitrogen (blue).

surface area (497 m^2 g^{-1}) than PAF-407 (205 m^2 g^{-1}) and PAF-408 (137 m^2 g^{-1}), indicating that the tetrahedral geometry of TPA fragments may facilitate the formation of a porous framework structure.[61] The pore volumes were calculated to be 0.37, 0.24 and 0.19 cm^3 g^{-1} for PAF-406, PAF-407 and PAF-408, respectively. The adsorption isotherms of HATN-PAFs exhibit both type-I and type-IV characteristics, indicating that both microporous and mesoporous structures exist in HATN-PAFs.

The isotherms of PAF-406 showed rapid uptake at low relative pressures, which indicated the microporous features of PAF-406. The high specific surface area and porous structure are more favourable for photocatalytic reactions, due to the optimal exposure of active sites on the catalyst surface to reactants.[40,62–65] As shown in Fig. S10,† the pore size distributions of PAF-406, PAF-407 and PAF-408 are mainly concentrated at 1.14, 1.50 and 1.79 nm, respectively. Thermal gravimetric analysis (TGA) shows that HATN-PAFs have a relatively high degree of thermal stability (Fig. S11†). In addition, HATN-PAFs also showed high chemical stability in 3 M HCl and were insoluble in alcohols (*e.g.* CH_3OH and C_2H_5OH), *N*,*N*-dimethylformamide (DMF), tetrahydrofuran (THF), haloalkanes (*e.g.* CH_2Cl_2 and $CHCl_3$) and other common organic solvents. Powder X-ray diffraction (PXRD) analysis reveals that HATN-PAFs are amorphous (Fig. S12†). Scanning electron microscopy (SEM) and transmission electron microscopy (TEM) analysis shows that the morphologies of HATN-PAFs all involve irregular particles (Fig. 1d, e and S13†). Meanwhile, it is observed that carbon and nitrogen in PAF-406 are evenly distributed throughout the polymer skeleton based on TEM elemental mapping (Fig. 1f).

Optical and electrochemical properties

The optical properties of HATN-PAFs are analysed using diffuse ultraviolet-visible (UV-vis) spectroscopy. All these HATN-PAFs exhibit strong absorption in the visible-light region. In particular, PAF-406 exhibits an absorption edge at 800 nm (orange line), while the maximum absorption peak of PAF-406 is red-shifted compared to the other two PAF materials. (Fig. 2a). The optical bandgaps (E_g) of PAF-406, PAF-407, and PAF-408 were estimated to be 1.58, 1.60, and 1.69 eV, respectively, based on the corresponding Tauc plots (Fig. 2b). To further investigate the energy levels of the HATN-PAFs, VB-XPS tests are performed, which give valence band energies (E_{VB}) of 0.62, 1.23, and 1.08 eV for PAF-406, PAF-407, and PAF-408 (Fig. S14†). The corresponding conduction band energies (E_{CB}) are calculated to be −0.96, −0.37, and −0.61 eV according to the formula $E_{CB} = E_{VB} - E_g$ (Fig. 2c). These results indicate that the energy levels of HATN-PAFs can be easily adjusted by changing the electron-donating linkage fragments between HATN moieties. Furthermore, the efficiencies of photoinduced charge-carrier generation, separation and transport[66] over HATN-PAFs are investigated by electrochemical impedance spectroscopy (EIS), transient photocurrent and time-resolved fluorescence decay measurements.[67,68] As can be seen from the EIS spectra (Fig. 2d), PAF-406 has smaller charge transfer resistance, indicating the faster migration of photogenerated charge carriers.[69] The transient photocurrent response of HATN-PAFs is measured based on switching cycles under Xe lamp irradiation. As shown in Fig. 2e, PAF-406 has the highest photocurrent response intensity, demonstrating that PAF-406 exhibits more efficient separation of electron–hole pairs.[70] The lifetimes of photogenerated charge carriers over HATN-PAFs are

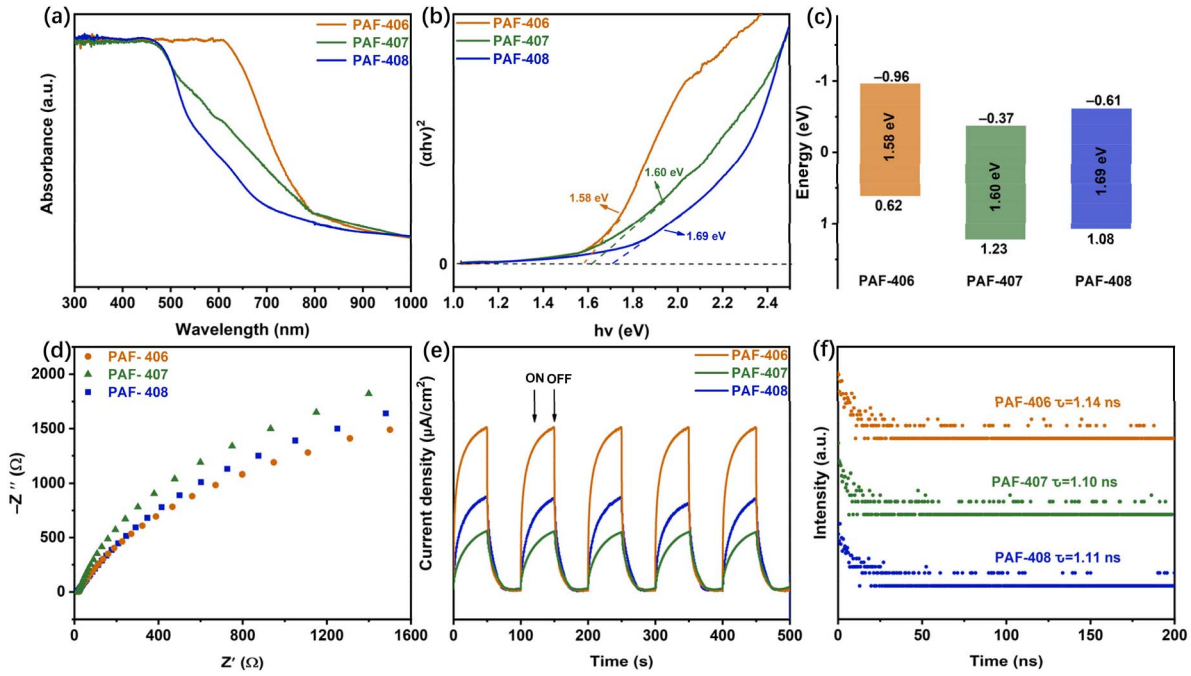

Fig. 2 (a) UV-vis spectra. (b) Tauc plots. (c) Experimentally determined band structures. (d) EIS spectra. (e) Transient photocurrent responses. (f) Time-resolved fluorescence spectra of HATN-PAFs.

evaluated by time-resolved photoluminescence (PL) attenuation spectroscopy (Fig. 2f). The average emission lifetimes of PAF-406, PAF-407, and PAF-408 are 1.14, 1.10, and 1.11 ns, respectively. Furthermore, PAF-406 possesses the lowest fluorescence emission intensity, implying that the recombination of photogenerated electron–hole pairs is suppressed in PAF-406 (Fig. S15†).[71] These observations indicate that PAF-406 exhibits superior properties for light harvesting, charge separation and migration, and suitable energy levels for the ORR, and it may potentially serve as a photocatalyst to produce the reactive oxygen species (ROS) that are essential for organic transformations.

Photosynthesis of 2-benzothiazoles

The photosynthesis of 2-benzothiazole derivatives over HATN-PAFs under visible light irradiation (λ = 460 nm, 24 W blue LED) is investigated. Initially, the photocatalytic synthesis of 2-phenylbenzothiazole from benzaldehyde and 2-aminothiophenol under an air atmosphere is studied as a model reaction to optimize the reaction conditions (Table 1). It is found that the PAF-406 catalyst exhibits the highest yield (99%) for this reaction compared with PAF-407 (90%) and PAF-408 (91%) under similar conditions (Table 1, entries 1–3). This is likely due to the more efficient photogenerated charge separation and transfer over the PAF-406 catalyst. In addition, the highest specific surface area of PAF-406 may ensure the optimal exposure of its active sites to reactants during photocatalysis.[40,62–65] The catalyst loading is also essential for the catalytic performance (Table 1, entries 4–6). Photocatalytic reactions using 2.0–4.0 mg of PAF-406 catalyst give 2-phenylbenzothiazole in >90% yield. The optimal reaction yield (99%) is obtained when 3.0 mg of PAF-406 catalyst is loaded. Increasing the catalyst loading results in a slightly lower yield (94%), probably due to the aggregation of the catalyst particles caused by the higher catalyst concentration which exposes insufficient active sites for photon capture and reactant contact.[72]

Table 1 Optimization of the reaction conditions[a]

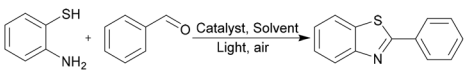

Entry	Catalyst	Solvent	Yield[b]
1	PAF-406 (3.0 mg)	CH_3OH	99%
2	PAF-407 (3.0 mg)	CH_3OH	90%
3	PAF-408 (3.0 mg)	CH_3OH	91%
4	PAF-406 (1.0 mg)	CH_3OH	41%
5	PAF-406 (2.0 mg)	CH_3OH	90%
6	PAF-406 (4.0 mg)	CH_3OH	94%
7	PAF-406 (3.0 mg)	Hexane	25%
8	PAF-406 (3.0 mg)	CH_3CN	38%
9	PAF-406 (3.0 mg)	DMF	35%
10	PAF-406 (3.0 mg)	CH_2Cl_2	48%

[a] 2-Aminothiophenol (0.5 mmol), benzaldehyde (0.5 mmol), HATN-PAF photocatalyst, solvent (3 mL), air, blue LED (460 nm, 24 W), 298 K, 3 h. [b] Isolated yield.

Additionally, the effects of the solvent on the reaction yield are then tested. Reactions in aprotic solvents, such as *N*,*N*-dimethylformamide (DMF), acetonitrile (CH_3CN), hexane and CH_2Cl_2, give 2-phenylbenzothiazole in lower yields (25–48%, Table 1, entries 7–10) than the analogous reaction in methanol (99%). These experiments illustrate that the optimal reaction conditions for 2-arylbenzothiazole photosynthesis catalysed by HATN-PAFs are as follows: 2-aminothiophenol (0.5 mmol) and benzaldehyde (0.5 mmol) as the reaction substrates, PAF-406 (3.0 mg) as the photocatalyst, CH_3OH as the reaction solvent, and a 24 W blue LED as the light source under an air atmosphere at 298 K for 3 h.

To study the reaction mechanism of the photosynthesis of 2-arylbenzothiazole over PAF-406, a series of control experiments was conducted (Fig. 3a). It is found that 2-phenylbenzothiazole formation is inhibited in the absence of light or air. However, a small amount of product (10%) can be isolated from the reaction without any photocatalyst, which may be attributed to the photoinduced self-coupling of 2-aminothiophenol. The *in situ* generated disulfide compound may serve as a photosensitizer to facilitate the generation of key reactive oxygen species, which promote 2-phenylbenzothiazole formation.[73] This reaction pathway seems not to be dominant in our catalytic system (Scheme S7 and Fig. S16†). These results illustrated that the HATN-PAF photocatalyst, light and air are all necessary in the current photocatalytic system. To better elucidate the presence of reactive oxygen species, (2,2,6,6-tetramethylpiperidin-1-yl) oxyl (TEMPO), 1,4-benzoquinone (BQ) and β-carotene are added to the current catalytic system as scavengers of free radicals, superoxide radical anions ($O_2^{\bullet-}$) and singlet oxygen ($^1O_2$), respectively, resulting in a partial decrease in reaction yields (24–36%). This indicates that $O_2^{\bullet-}$ and $^1O_2$ are generated over PAF-406 under light irradiation under an air atmosphere, which

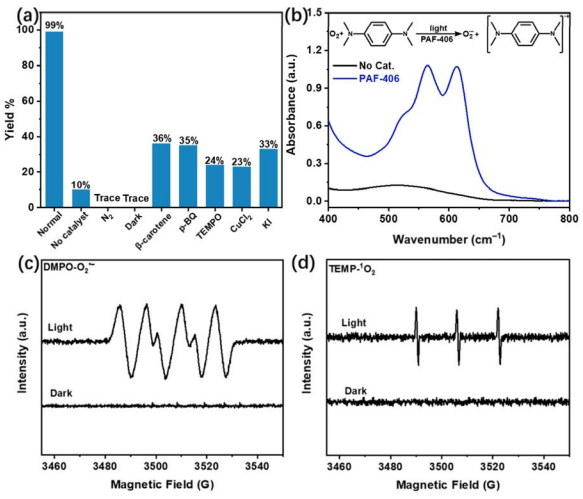

Fig. 3 (a) Control experiments using the PAF-406 catalyst under various conditions and (b) UV-vis absorption spectra of TMPD in CH_3OH in the absence (black curve) and presence (blue curve) of PAF-406 under light irradiation in open air. ESR spectra from DMPO-$O_2^{\bullet-}$ (c) and TEMP-$^1O_2$ (d) trapping experiments in the presence of PAF-406 under light irradiation.

act as key ROS for the synthesis of 2-arylbenzothiazole. Furthermore, the presence of PAF-406 facilitates the single electron transfer process from *N*,*N*,*N*′,*N*′-tetramethyl-*p*-phenylenediamine (TMPD) to molecular oxygen with the formation of nitrogen cationic radicals and superoxide radicals under light irradiation (Fig. 3b).[74] The generation of $O_2^{\bullet-}$ and $^1O_2$ in the current catalytic system is also confirmed by *in situ* electron spin resonance (ESR) analysis of radical trapping experiments (Fig. 3c and d). Moreover, the reaction yields are severely inhibited when the photoexcited electron (e^-) scavenger $CuCl_2$ and the photogenerated hole (h^+) scavenger KI are respectively added to the current photocatalytic system (Fig. 3a). This indicates that h^+ and e^- are also involved in the current photocatalytic reaction process.

As $Pd(PPh_3)_4$ was used as a catalyst for the synthesis of HATN-PAFs, the possible effect of residual Pd species on the photocatalytic performance for 2-phenylbenzothiazole synthesis should be tested. As can be seen from inductively coupled plasma atomic emission spectrometry (ICP-AES) analysis, a trace amount of Pd (0.2–0.4 wt%) remains in HATN-PAFs (Table S1†). This could also be observed by TEM element mapping and EDS elemental analysis of PAF-406 (Fig. S17 and S18†). Furthermore, a series of control experiments based on Pd-loaded PAF-406 catalytic systems is performed to verify the role of residual Pd on the photosynthesis of 2-phenylbenzothiazole. It is shown that a higher Pd species content in the HATN-PAF photocatalysts does not seem to positively affect their performance in the current photocatalytic system (Fig. S19†).

Based on these experimental observations, a possible reaction mechanism for the photosynthesis of 2-arylbenzothiazole over PAF-406 is proposed (Fig. 4).[27,29] The substrate molecules 2-aminothiophenol and benzaldehyde initially undergo a condensation reaction to form the imine intermediate I, which subsequently cyclizes to form intermediate II. Under light irradiation, energy transfer (ET) to absorbed oxygen molecules over PAF-406 could occur to produce reactive $^1O_2$ (Fig. 4, Path A), which can oxidize intermediate II to give intermediate III. β-H elimination affords the 2-arylbenzothiazole product accompanied by the generation of hydrogen peroxide as a byproduct. Conversely, light excitation could also lead to the separation of an electron–hole pair over the PAF-406 photocatalyst (Fig. 4, Path B). In this case, several single electron transfer (SET) processes could be involved. The photogenerated electron could undergo an oxygen reduction reaction (ORR) to give the reactive oxygen species $O_2^{\bullet-}$. Simultaneously, the photogenerated holes could serve as strong oxidizing sites to oxidize intermediate II to generate the cationic radical intermediate IV, which could be deprotonated by the generated $O_2^{\bullet-}$ giving the radical intermediate V and HOO$^\bullet$. Hydrogen atom abstraction from intermediate V by HOO$^\bullet$ ultimately resulted in the product 2-arylbenzothiazole and H_2O_2 as a byproduct. We believe that these two reaction pathways would jointly accelerate the overall photosynthesis of the 2-arylbenzothiazole product.

Subsequently, the substrate scope for the photosynthesis of benzothiazoles over PAF-406 is investigated under the optimized conditions (Table 2). It is found that a series of benzaldehyde derivatives featuring both electron-withdrawing and electron-donating substituents are compatible with the current photocatalytic system. The highest yield of benzothiazole product **3a** of 99% is achieved from the photocatalytic reaction using an unsubstituted benzaldehyde as the starting material. It is clearly observed that steric effects related to the substituents on the benzaldehyde play a major role in determining the reaction yields. The reaction yields obtained for isomers substituted at different positions are in the order: *ortho*- (**3b–3d**) < *meta*- (**3e–3g**, **3k**) < *para*- (**3h–3j**, **3l**) substitution. Similarly, the reaction using a *para*-CH_3-substituted benzaldehyde affords the corresponding 2-arylbenzothiazole product **3l** in 98% yield, which is higher than its *meta*-substituted isomer **3k** (91%). In addition, –OCH_3- and –CN-substituted benzaldehydes can be converted to the target products **3m** and **3n** in 91% and 95% yields, respectively. The reaction using butyl aldehyde gives 2-butylbenzothiazole (**3o**) in 91% yield. Notably, heterocycle-substituted aldehydes are also suitable as substrates for this reaction, from which the target molecules **3p–3r** are isolated in high yields (93–99%). Additionally, the –Br-

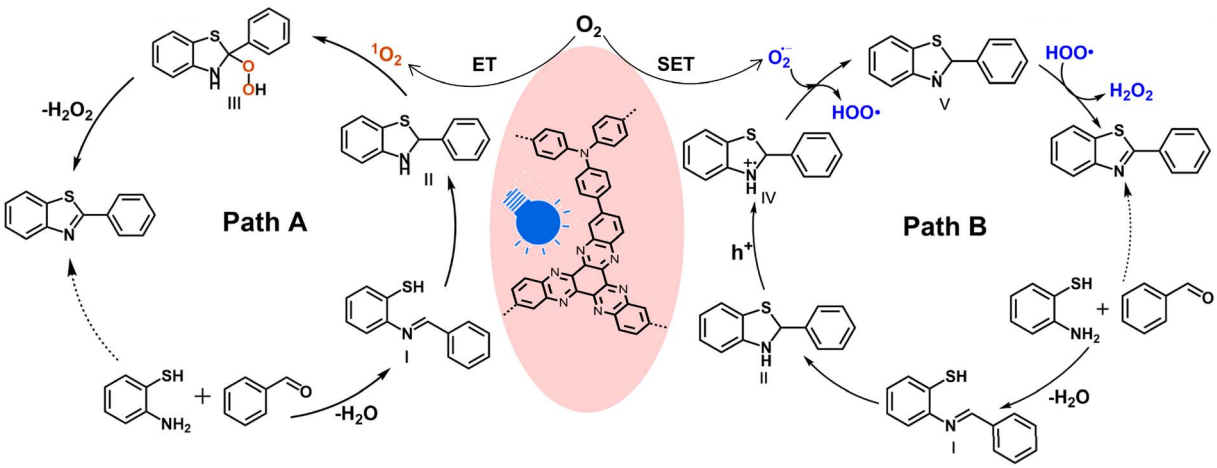

Fig. 4 The possible reaction mechanism of the photosynthesis of 2-arylbenzothiazole over PAF-406.

Table 2 The photosynthesis of benzothiazoles catalysed by PAF-406.[a,b]

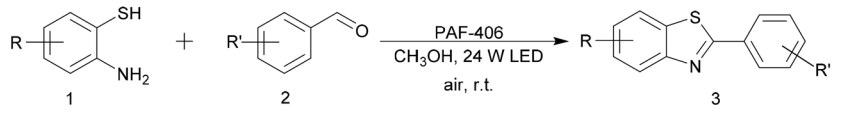

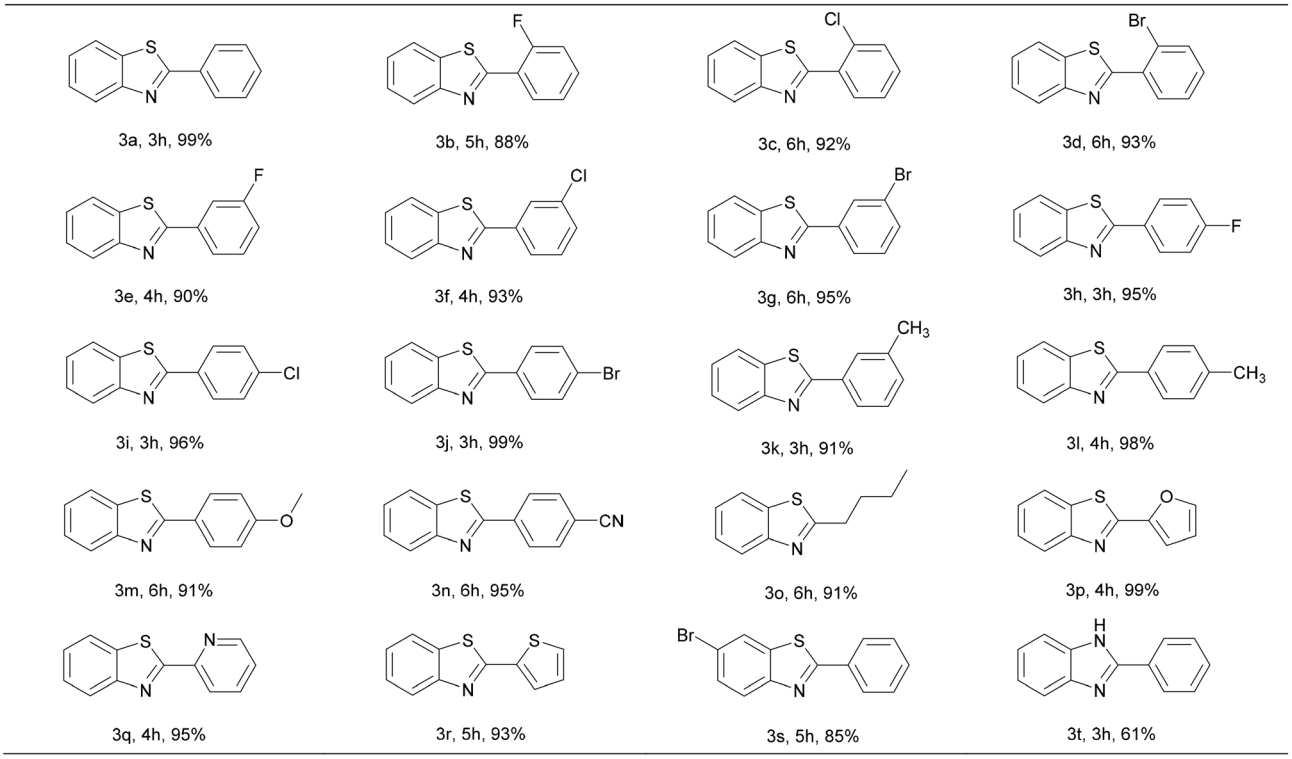

[a] Reaction conditions: photocatalyst PAF-406 (3.0 mg), 2-aminothiophenol (0.5 mmol), aldehyde (0.5 mmol), CH_3OH (3.0 mL), air, blue LED (460 nm, 24 W), 298 K. [b] Isolated yield.

substituted 2-aminothiophenol reacts with benzaldehyde giving the product **3s** in 85% yield. Under similar conditions, the photosynthesis of 2-phenylbenzimidazole **3t** from *o*-phenylenediamine and benzaldehyde using the current photocatalytic system only achieves a moderate yield (61%). Overall, the PAF-406-based photocatalytic system exhibits excellent catalytic efficiency for the photosynthesis of benzothiazoles under ambient conditions, which is superior to reported organic semiconductor photocatalysts and comparable to metal-based heterogeneous photocatalysts and organo-based homogeneous photocatalysts (Table S2†).[25–29] While thermal catalysis can also achieve this reaction with high efficiency, this is possible in the presence of organic additives or metal catalysts, which are not recyclable.[10–21] The recyclability and scalability of the current photocatalyst are tested. We found that the photocatalytic activity of PAF-406 does not significantly decrease after recycling for 10 cycles (Fig. S20†). To our delight, the recycled PAF-406 also maintained its original structure, demonstrating its excellent recyclability. Last but not least, the gram-scale synthesis of benzothiazole is also performed. In a typical experiment 1.6 g of product **3a** was isolated in 97% yield, indicating that the current photocatalytic system is scalable.

Conclusions

We present the rational design and synthesis of D–A-type PAFs consisting of HATN units for the photocatalytic synthesis of 2-benzothiazoles. The porosity, photoelectric properties, energy levels, and band gaps of HATN-PAFs can be readily tuned by adjusting the linkage fragments. Among these HATN-PAFs, the combination of HATN with TPA fragments facilitates photoinduced charge carrier separation and transfer. The energy levels are suitable for the oxygen reduction reaction to generate the reactive oxygen species $O_2^{\bullet-}$ and $^1O_2$, which may jointly accelerate the oxidative formation of the final 2-benzothiazole products. Moreover, the robust character of C–C bonding allows for excellent durability. These unique features render HATN-PAFs with excellent performance for the photosynthesis of 2-benzothiazoles in terms of catalytic efficiency, substrate adaptability and catalyst recyclability, and reactions do not need pure oxygen as an oxidant. This study highlights that the rational design of PAF catalytic materials based on HATN fragments could afford efficient photocatalysts for benzothiazole synthesis.

Data availability

The data that support the findings of this study are available in the ESI.†

Author contributions

X. Tao conceived and designed this work. J. Shao conducted the synthesis and characterization of the materials and wrote this paper. H. Wang helped with the characterization of the materials and the data analysis. All authors reviewed and edited the manuscript.

Conflicts of interest

There are no conflicts to declare.

Acknowledgements

Financial supports from the National Natural Science Foundation of China (grant no. 52173195) and Jilin Provincial Department of Science and Technology (grant no. 20250205071GH) are gratefully acknowledged.

Notes and references

1 C. S. W. Law and K. Y. Yeong, *Expert Opin. Ther. Pat.*, 2022, **32**, 299–315.
2 R. S. Keri, M. R. Patil, S. A. Patil and S. Budagumpi, *Eur. J. Med. Chem.*, 2015, **89**, 207–251.
3 S. Tariq, P. Kamboj and M. Amir, *Arch. Pharm.*, 2019, **352**, 1800170.
4 N. Pathak, E. Rathi, N. Kumar, S. G. Kini and C. M. Rao, *Mini-Rev. Med. Chem.*, 2020, **20**, 12–23.
5 M. Gjorgjieva, T. Tomašič, D. Kikelj and L. P. Mašič, *Curr. Med. Chem.*, 2018, **25**, 5218–5236.
6 G. Kumar and N. P. Singh, *Bioorg. Chem.*, 2021, **107**, 104608.
7 A. Irfan, F. Batool, S. A. Zahra Naqvi, A. Islam, S. M. Osman, A. Nocentini, S. A. Alissa and C. T. Supuran, *J. Enzyme Inhib. Med. Chem.*, 2020, **35**, 265–279.
8 N. Bhattarai, A. A. Kumbhar, Y. R. Pokharel and P. N. Yadav, *Mini-Rev. Med. Chem.*, 2021, **21**, 2996–3029.
9 N. A. Al-Masoudi, N. Jafar, L. J. Abbas, S. J. Baqir and C. Pannecouque, *Z. Naturforsch., B*, 2011, **66**, 953–960.
10 L. Liu, C. Tan, R. Fan, Z. Wang, H. Du, K. Xu and J. Tan, *Org. Biomol. Chem.*, 2019, **17**, 252–256.
11 A. B. Khemnar and B. M. Bhanage, *RSC Adv.*, 2014, **4**, 8939–8942.
12 H.-Q. Do and O. Daugulis, *J. Am. Chem. Soc.*, 2007, **129**, 12404.
13 T. Xiao, S. Xiong, Y. Xie, X. Dong and L. Zhou, *RSC Adv.*, 2013, **3**, 15592–15595.
14 K. Inamoto, C. Hasegawa, J. Kawasaki, K. Hiroya and T. Doi, *Adv. Synth. Catal.*, 2010, **352**, 2643.
15 M. Okimoto, T. Yoshida, M. Hoshi, K. Hattori, M. Komata, K. Tomozawa and T. Chiba, *Heterocycles*, 2008, **75**, 35–42.
16 S. Sharma and A. Sharma, *Org. Biomol. Chem.*, 2019, **17**, 4384–4405.
17 M. Shaw, J. Twilton and D. Macmillan, *J. Org. Chem.*, 2016, **16**, 6898–6926.
18 S. Sharma, R. S. Pathare, A. K. Maurya, K. Gopal, T. K. Roy, D. M. Sawant and R. T. Pardasani, *Org. Lett.*, 2016, **18**, 356–359.
19 W. Sun, H. Chen, K. Wang, X. Wang, M. Lei, C. Liu and Q. Zhong, *J. Mol. Catal.*, 2021, **510**, 111693.
20 Z.-J. Yang, Q.-T. Gong, Y. Yu, W.-F. Lu, Z.-N. Wu, N. Wang and X.-Q. Yu, *J. Bioorg. Chem.*, 2021, **107**, 104607.
21 A. A. Heredia, J. E. Argüello and L. C. Schmidt, *J. Org. Biomol. Chem.*, 2024, **22**, 1064–1072.
22 S. Das, S. Samanta, S. K. Maji, P. K. Samanta, A. K. Dutta, D. N. Srivastava, B. Adhikary and P. Biswas, *Tetrahedron Lett.*, 2013, **54**, 1090–1096.
23 A. R. Wade, H. R. Pawar, M. V. Biware and R. C. Chikate, *Green Chem.*, 2015, **17**, 3879–3888.
24 M. Koohgard, Z. Hosseinpour, A. M. Sarvestani and M. Hosseini-Sarvari, *Catal. Sci. Technol.*, 2020, **10**, 1401–1407.
25 H. Liu, Q. Li, P. Pan, L. Zhou, B. Deng, S. Zhao, P. Liu, Y. Wang and J. Li, *Chin. Chem. Lett.*, 2023, **34**, 108562.
26 S. Li, J. Yin, H. Zhang and K. A. Zhang, *ACS Appl. Mater. Interfaces*, 2023, **15**, 2825–2831.
27 Y. Zhu, S. Li, X. Yang, S. Wang and Y. Zhang, *J. Mater. Chem. A*, 2022, **10**, 13978–13986.
28 Z. Liu, Z. Chen, H. Tong, M. Ji and W. Chu, *Green Chem.*, 2023, **25**, 5195–5205.
29 W. Wang, Y. Bai, Z. Li, Q. Su, B. Li, M. Lei, J. Feng, A. Xu and Q. Wu, *Chem. Eng. J.*, 2024, **501**, 157486.
30 Y. Yuan and G. - Zhu, *ACS Cent. Sci.*, 2019, **5**, 409–418.
31 T. Ben, H. Ren, S. Ma, D. Cao, J. Lan, X. Jing, W. Wang, J. Xu, F. Deng, J. M. Simmons, S. Qiu and G. Zhu, *Angew. Chem., Int. Ed.*, 2009, **48**, 9457–9460.
32 N. B. McKeown, S. Makhseed and P. M. Budd, *Chem. Commun.*, 2002, 2780–2781.
33 Y. Tian and G. Zhu, *Chem. Rev.*, 2020, **120**, 8934–8986.
34 S. Ghosh, D. Sarkar, S. Bastia and Y. S. Chaudhary, *Nanoscale*, 2023, **15**, 10939–10974.
35 H. Wang, X. Xu, L. Cao, Z. Zhang, J. Li, X. Liu, X. Tao and G. Zhu, *EES. Catal.*, 2024, **2**, 1100–1110.
36 X. Xu, H. Wang, Z. Zhang, J. Li, X. Liu, X. Tao and G. Zhu, *Nanoscale*, 2024, **16**, 11138–11145.
37 L. Cao, C. Wang, H. Wang, X. Xu, X. Tao, H. Tan and G. Zhu, *Angew. Chem., Int. Ed.*, 2024, **63**, e202402095.
38 M. Cheng, H. Wang, L. Cao, J. Shao, Y. He, X. Tao and G. Zhu, *ChemCatChem*, 2024, e202401141.
39 J. Song, H. Lei, Y. Zhai, Z. Dou, Y. Ding, X. Han, Y. Tian, F. Cui and G. Zhu, *Chem. Sci.*, 2024, **15**, 15717–15724.
40 N. Yin, W. Chen, Y. Yang, Z. Tang, P. Li, X. Zhang, L. Tang, T. Wang, Y. Wang, Y. Zhou and Z. Zou, *Chin. J. Catal.*, 2023, **51**, 168–179.
41 J. Wang, X. Zhang, Z. Liu, J. Yu, H.-G. Wang, X.-L. Wu, F. Cui and G. Zhu, *Angew. Chem., Int. Ed.*, 2024, **63**, e202401559.
42 P. T. Parvatkar, S. Kandambeth, A. C. Shaikh, I. Nadinov, J. Yin, V. S. Kale, G. Healing, A.-H. Emwas, O. Shekhah,

H. N. Alshareef, O. F. Mohammed and M. Eddaoudi, *J. Am. Chem. Soc.*, 2023, **145**, 5074–5082.
43 B. Jothi, A. David Stephen Arputharaj, K. Selvaraju, S. Lara Priyadharshini and A. S. Abdullah G, *ChemistrySelect*, 2024, **9**, e202304156.
44 J. Chu, Z. Liu, J. Yu, L. Cheng, H. Wang, F. Cui and G. Zhu, *Angew. Chem.*, 2024, **136**, e202314411.
45 N. Miyaura, T. Yanagi and A. Suzuki, *Synth. Commun.*, 1981, **11**, 513–519.
46 Y. Yuan, F. Sun, H. Ren, X. Jing, W. Wang, H. Ma, H. Zhao and G. Zhu, *J. Mater. Chem.*, 2011, **21**, 13498–13502.
47 Y. Yan, X. Jia, M. Feng, C. Wang and D. Chao, *J. Polym. Sci., Part A: Polym. Chem.*, 2017, **55**, 1669–1673.
48 Y. Hu, Y. Ji, Z. Qiao and L. Tong, *Microporous Mesoporous Mater.*, 2023, **362**, 112767.
49 P. Xu, S. Ouyang, Q. Bai, Q. Ma and Y. Zhu, *J. Polym. Sci.*, 2024, **62**, 1647–1653.
50 J. Wang, C.-S. Chen and Y. Zhang, *ACS Sustain. Chem. Eng.*, 2018, **6**, 1772–1779.
51 X. Cao, Y. Zhao, J. Leng, X. Bai, Y. Qu, L. Jiang, D. Chen and J. Wang, *Chem. Synth.*, 2025, **5**, 5.
52 L. Zhang, R. Wang, Z. Liu, J. Wan, S. Zhang, S. Wang, K. Hua, X. Liu, X. Zhou, X. Luo, X. Zhang, M. Cao, H. Kang, C. Zhang and Z. Guo, *Adv. Mater.*, 2023, **35**, 2210082.
53 Y. Dai, W. Li, Z. Chen, X. Zhu, J. Liu, R. Zhao, D. S. Wright, A. Noori, M. F. Mousavi and C. Zhang, *J. Mater. Chem. A*, 2019, **7**, 16397–16405.
54 M. Surendranath, R. Ramesan, P. Nair and R. Parameswaran, *ACS Appl. Bio Mater.*, 2024, **7**, 7429–7443.
55 X. Dong, Y. Wang, F. Huang and X. Lang, *Chem. Eng. J.*, 2023, **469**, 143934.
56 M. Kotp, N. Torad, J. Lüder, A. El-Amir, W. Chaikittisilp, Y. Yamauchi and A. EL-Mahdy, *J. Mater. Chem. A*, 2023, **11**, 764–774.
57 R. Xiao, J. M. Tobin, M. Zha, Y. L. Hou, J. He, F. Vilela and Z. Xu, *J. Mater. Chem. A*, 2017, **5**, 20180–20187.
58 S. Sau, F. Banerjee and S.-K. Samanta, *ACS Appl. Nano Mater.*, 2023, **6**, 11679–11688.
59 X. Yang, L. Duan, X. Ran, B. Ran and S. Yi, *J. Polym. Res.*, 2022, **29**, 499.
60 S. Zhang, G. Cheng, L. Guo, N. Wang, B. Tan and S. Jin, *Angew. Chem., Int. Ed.*, 2020, **59**, 6007–6014.
61 F. Li, X. Dai, L. Zhang, H. Wu, J. Li, J. Guo and Q. Yi, *Fuel*, 2024, **370**, 131812.
62 H. Xu, X. Li, H. Hao, X. Dong, W. Sheng and X. Lang, *Appl. Catal., B*, 2021, **285**, 119796.
63 T. Huang, J. Kou, H. Yuan, H. Guo, K. Yuan, H. Li, F. Wang and Z. Dong, *Adv. Funct. Mater.*, 2025, **35**, 2413943.
64 Z. Gu, J. Wang, Z. Shan, M. Wu, T. Liu, L. Song, G. Wang, X. Ju, J. Su and G. Zhang, *J. Mater. Chem. A*, 2022, **10**, 17624–17632.
65 Y.-Y. Gu, J. Wang, Q. Tang, H. Wei, J. Ning, X. Lan, X. Wang, X. Li, Y. Jia, S. Wang and L. Hao, *ACS Catal.*, 2024, **14**, 11262–11272.
66 C. Qin, X. Wu, L. Tang, X. Chen, M. Li, Y. Mou, B. Su, S. Wang, C. Feng, J. Liu, X. Yuan, Y. Zhao and H. Wang, *Nat. Commun.*, 2023, **14**, 5238.
67 C. Cheng, B. He, J. Fan, B. Cheng, S. Cao and J. Yu, *Adv. Mater.*, 2021, **33**, 2100317.
68 S. Cao, B. Shen, T. Tong, J. Fu and J. Yu, *Adv. Funct. Mater.*, 2018, **28**, 1800136.
69 M. Kou, Y. Wang, Y. Xu, L. Ye, Y. Huang, B. Jia, H. Li, J. Ren, Y. Deng, J. Chen, Y. Zhou, K. Lei, L. Wang, W. Liu, H. Huang and T. Ma, *Angew. Chem., Int. Ed.*, 2022, **61**, e202200413.
70 H. Cheng, H. Lv, J. Cheng, L. Wang, X. Wu and H. Xu, *Adv. Mater.*, 2022, **34**, 2107480.
71 M. Liu, J. Liu, K. Zhou, J. Chen, Q. Sun, Z. Bao, Q. Yang, Y. Yang, Q. Ren and Z. Zhang, *Adv. Sci.*, 2021, **8**, 2100631.
72 M. Ahmad, W. Rehman, M. M. Khan, M. T. Qureshi, A. Gul, S. Haq, R. Ullah, A. Rab and F. Menaa, *J. Environ. Chem. Eng.*, 2021, **9**, 104725.
73 H. Hwang, S. Lee, S. Han, Y. Moon, Y. You and E. Cho, *J. Org. Chem.*, 2020, **85**, 11835–11843.
74 M. Jiang, X.-L. Li, N. Han, X.-Y. Yao, F.-D. Wang, K.-K. Niu, H. Liu, S. Yu and L.-B. Xing, *Chem. Synth.*, 2025, **5**, 6.